NEAR-INFRARED IMAGING POLARIMETRY OF GGD 27: CIRCULAR POLARIZATION AND MAGNETIC FIELD STRUCTURES

Jungmi Kwon[1,2,3,7], Motohide Tamura[1,2], James H. Hough[4], Tetsuya Nagata[5], Nobuhiko Kusakabe[2], and Hiro Saito[6]

[1] Department of Astronomy, Graduate School of Science, The University of Tokyo, 7-3-1 Hongo, Bunkyo-ku, Tokyo 113-0033, Japan; jungmi.kwon@astron.s.u-tokyo.ac.jp
[2] National Astronomical Observatory of Japan, 2-21-1 Osawa, Mitaka, Tokyo 181-8588, Japan
[3] Institute of Space and Astronautical Science, Japan Aerospace Exploration Agency, 3-1-1 Yoshinodai, Chuo-ku, Sagamihara, Kanagawa 252-5210, Japan
[4] University of Hertfordshire, Hatfield, Herts AL10 9AB, UK
[5] Kyoto University, Sakyo-ku, Kyoto 606-8502, Japan
[6] Department of Astronomy and Earth Sciences, Tokyo Gakugei University, Koganei, Tokyo 184-8501, Japan

ABSTRACT

Near-infrared imaging polarimetry in the J, H, and K_s bands was carried out for GGD 27 in the dark cloud Lynds 291. Details of an infrared reflection nebula associated with the optical nebulosity GGD 27 and the infrared nebula GGD 27 IRS are presented. Aperture photometry of 1263 point-like sources, detected in all three bands, was used to classify them based on a color–color diagram, and the linear polarization of several hundred sources was determined, with the latter used to map the magnetic field structure around GGD 27. This field, around GGD 27 IRS, appears to be associated with the extended CO outflow of IRAS 18162–2048; however, there are partly distorted or bent components in the field. The Chandrasekhar–Fermi method gives an estimate of the magnetic field strength as ∼90 μG. A region associated with GGD 27 IRS is discovered to have a circular polarization in the range of ∼2%–11% in the K_s band. The circular polarization has an asymmetric positive/negative pattern and extends out to ∼ 120″ or 1.0 pc. The circular and linear polarization patterns are explained as resulting from a combination of dense inner and fainter outer lobes, suggesting episodic outflow.

Key words: circumstellar matter – infrared: stars – ISM: individual objects (GGD 27) – ISM: structure – polarization – stars: formation

Supporting material: machine-readable tables

1. INTRODUCTION

The giant molecular cloud complex Lynds 291 in Sagittarius (Lynds 1962) is a site of active star formation, with approximate dimensions of 20 pc × 80 pc, located at a distance of approximately 1.7 kpc. The mass of the cloud is approximately $1.3 \times 10^5 M_\odot$ in ^{12}CO. The northern part of the cloud is dominated by the H II region IC 1284 and the two reflection nebulae NGC 6589 and NGC 6595. The southwestern edge of the cloud consists of a high extinction ridge with numerous dense cores that are being compressed by an expanding H I bubble energized by OB stars and possibly by several past supernova explosions. Star formation is active all along the ridge. A well studied source is IRAS 18162–2048, which drives the luminous Herbig–Haro objects HH 80–81. The HH 80–81 system, discovered by Reipurth & Graham (1988) as a highly collimated radio continuum jet, extends out to 18.4 pc (Masqué et al. 2012) at an angular position of 20° (Martí et al. 1993).

One important part of the Lynds 291 cloud is the region around the reflection nebula GGD 27 and the Herbig–Haro objects HH 80–81. This region contains several young stellar objects (YSOs) and outflows, which are often associated with infrared nebulosity. The optical nebula GGD 27, located at the southwestern edge of a dark lane extending in the northwest–southeast direction of Sagittarius, exhibits CO bipolar flow corresponding to the HH 80–81 system with blue- and redshifted lobes extending, from the central source, 2.3 pc to the south and 3 pc to the north. It has a circumstellar disk

elongated in the east–west direction (Yamashita et al. 1987). Near GGD 27 lies the infrared reflection nebula GGD 27 IRS discovered by Yamashita et al. (1987). They used K-band aperture mapping polarimetry with a beam of 8″ to show that the illuminating source of the infrared reflection nebula is IRS 2 (IRAS 18162–2048). Tamura et al. (1991) and Aspin et al. (1991) performed K- and H-band imaging polarimetry with infrared arrays of 0.″78 and 0.″6 pixel^{-1}, much higher spatial resolution than that of Yamashita et al. (1987). All three previous polarimetric studies covered a relatively limited field of view of no more than ∼ 150″ × 110″.

In recent years, imaging linear polarimetry has been used widely to investigate the environments of YSOs, while imaging circular polarimetry has been used far less. Our previous studies, which have included a systematic near-infrared survey of circular polarization in star-forming regions of various luminosities, presented the relationships between luminosities, extents, and the degree of circular polarization. We found that a high degree of circular polarization, generated in some star-forming regions, was consistent with a dichroic extinction mechanism (Chrysostomou et al. 2007; Fukue et al. 2009; Kwon et al. 2013, 2014). Therefore, it is important to extend this survey for various star-forming regions, in particular bipolar nebulae such as GGD 27 IRS, and to determine how often significant circular polarization is observed.

In this paper, new deep- and wide-field near-infrared imaging polarimetry for GGD 27 IRS is presented, as part of an ongoing JHK_s polarimetry survey of star-forming regions. The observations are described in Section 2 and the data analysis in Section 3. The results of imaging and aperture polarimetry are presented in Section 4, and the magnetic field
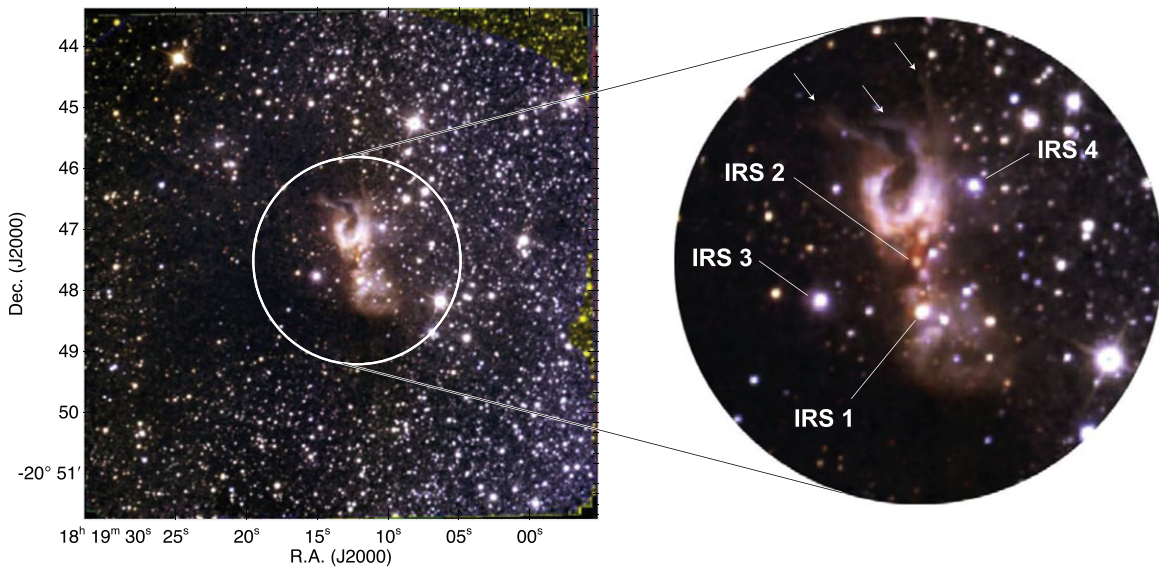
---

[7] JSPS Postdoctoral Fellow.

Figure 1. Color composite Stokes I image of the GGD 27 IRS region in the J (blue), H (green), and K_s (red) bands from IRSF/SIRPOL observations. The thin red, green, and blue lines around the perimeter are the boundaries of the Stokes I images associated with each band. There are bad pixel clusters near the upper left and upper right corners and near the middle of the right boundary. See Tamura et al. (1991) and Aspin et al. (1991) for the identification of other notable infrared sources. The inset shows the bright inner shell with a U-shape in the northern lobe and a bright knot, a part of the bright inner shell, in the southern lobe. Arrows indicate nebulosity tails discussed in Section 4.2.

Table 1
Photometry of Point-like Sources in the GGD 27 IRS Region

Source	Position		J (mag)	H (mag)	K_s (mag)	Group[a]
	$\alpha_{J2000.0}$	$\delta_{J2000.0}$				
1	18 19 12.76	$-20\ 51\ 36.0$	12.666 ± 0.003	11.060 ± 0.001	10.453 ± 0.002	A
2	18 19 27.92	$-20\ 51\ 35.8$	16.068 ± 0.039	13.779 ± 0.008	12.928 ± 0.014	A
3	18 19 28.70	$-20\ 51\ 35.1$	13.959 ± 0.006	13.539 ± 0.005	13.434 ± 0.024	A
4	18 19 28.32	$-20\ 51\ 34.4$	14.962 ± 0.011	12.755 ± 0.002	11.801 ± 0.004	A
5	18 19 14.25	$-20\ 51\ 34.1$	15.628 ± 0.029	14.390 ± 0.014	13.831 ± 0.027	A

Note. Units of right ascension are hours, minutes, and seconds, and units of declination are degrees, arcminutes, and arcseconds. Positions are from the J–H–K_s image (Figure 1).
[a] Classification based on a color–color diagram (see Section 4.1.1).

(This table is available in its entirety in machine-readable form.)

structure related to the star-forming activity in the GGD 27 IRS region is discussed, together with the illuminating sources for the infrared reflection nebulae. In addition, the results of circular polarimetry of GGD 27 IRS are presented for the first time. A concluding summary is given in Section 5.

2. OBSERVATIONS

Observations in the direction of GGD 27 IRS were carried out using the SIRPOL imaging polarimeter at the Infrared Survey Facility (IRSF) 1.4 m telescope at SAAO in South Africa. It consists of a single-beam polarimeter (an achromatic half-wave plate rotator unit and a polarizer) and an imaging camera (Nagayama et al. 2003). The camera, SIRIUS, has three 1024×1024 HgCdTe IR detectors. The Facility enables deep wide-field ($7.'7 \times 7.'7$ at a scale of $0.''453\ \text{pixel}^{-1}$) simultaneous imaging polarimetry in the JHK_s bands (Kandori et al. 2006).

Linear polarimetry was performed on the night of 2006 March 14. Exposures of ten seconds were made at four wave-plate angles ($0°$, $45°$, $22.°5$, and $67.°5$) at 10 dithered positions per set. The same sequence of observations was repeated three times for the target object and for the sky background to

increase the signal-to-noise ratio (S/N). The total integration time was 300 s per wave-plate angle. The typical seeing (the full width at half-maximum of the point-spread function) was approximately $1.''5$ (~ 3.3 pixels) in the J band.

In addition to the linear polarimetry observations, IRSF/ SIRPOL was used to make circular polarimetry observations. To do this, SIRPOL was equipped with a stepped achromatic quarter-wave plate. An achromatic half-wave plate was continuously rotated above the quarter-wave plate, thereby smearing out any linear polarization present. The instrumental circular polarization was less than 0.3% for approximately 100% of incident linearly polarized light.

Circular polarimetry observations of the GGD 27 IRS regions were made on the nights of 2008 July 24 and 2014 March 21. Exposures of ten seconds were made at two wave-plate angles ($0°$ and $90°$) for 10 dithered positions per set, and the sequence of observations was repeated 21 times for the target object and for the sky background. The total integration time was 2100 s per wave-plate angle, and the stellar seeing size during the observations was $1.''5$–$1.''9$ (3.3–4.3 pixels) in the J band.

Table 2
Polarimetry of Point-like Sources in the GGD 27 IRS Region

Source	P_J (%)	P_H (%)	P_{K_s} (%)	θ_J (deg)	θ_H (deg)	θ_{K_s} (deg)
1	0.779 ± 0.28	1.098 ± 0.11	0.702 ± 0.20	157.74 ± 9.8	111.03 ± 2.9	113.31 ± 7.8
2	10.104 ± 4.33	2.014 ± 0.92	1.465 ± 1.49	51.55 ± 11.3	51.90 ± 11.9	161.31 ± 20.4
3	0.505 ± 0.60	1.123 ± 0.64	6.747 ± 2.68	132.48 ± 21.8	125.24 ± 14.2	39.12 ± 10.6
4	2.466 ± 1.29	1.140 ± 0.33	2.310 ± 0.56	126.84 ± 13.3	43.16 ± 7.9	57.44 ± 6.8
5	8.851 ± 2.91	1.439 ± 1.44	3.099 ± 3.10	103.53 ± 8.9	58.83 ± 55.4	160.63 ± 55.6

Note. In this paper, sources with $P/\delta P > 3$ are used.

(This table is available in its entirety in machine-readable form.)

The data were processed using IRAF in the conventional manner, including dark-field subtraction, flat-field correction, median sky subtraction, and frame registration. The remaining artificial stripe pattern was removed using IDL. The pixel coordinates of point-like sources found in the reduced images were matched with the celestial coordinates of their counterparts in the 2MASS point-source catalog (PSC). The IRAF IMCOORDS package was applied to the matched list to obtain plate transform parameters. The rms uncertainty in the coordinate transformation was approximately $0\rlap{.}{''}1$.

Figure 1 shows a JHK_s color composite Stokes I image of an $8\rlap{.}{'}0 \times 8\rlap{.}{'}0$ region around GGD 27 IRS. The observed field is slightly larger than the field of view of the camera because of dithering.

3. ANALYSIS

3.1. Photometry

The IRAF/DAOPHOT package was used for source detection (Stetson 1987). The DAOFIND program automatically detected point-like sources with peak intensities greater than 15σ above the local sky background, where σ is the rms uncertainty. The automatic detection procedure misidentified some spurious sources, which were removed by visual inspection. Then the IDL photometry package adapted from DAOPHOT was used to perform aperture photometry. An aperture radius of 4 pixels was used in all three bands, and the radius of the sky annulus was fixed at 10 pixels with a width of 5 pixels.

The Stokes I for each point-like source was calculated using

$$I = \frac{1}{2}(I_0 + I_{22.5} + I_{45} + I_{67.5}). \tag{1}$$

The color and magnitude of the photometry were transformed into the 2MASS system using

$$\mathrm{MAG_{2MASS}} = \mathrm{MAG_{IRSF}} + \alpha_1 \times \mathrm{COLOR_{IRSF}} + \beta_1 \tag{2}$$

and

$$\mathrm{COLOR_{2MASS}} = \alpha_2 \times \mathrm{COLOR_{IRSF}} + \beta_2 \tag{3}$$

where $\mathrm{MAG_{IRSF}}$ is the instrumental magnitude from the IRSF images and $\mathrm{MAG_{2MASS}}$ is the magnitude from the 2MASS PSC. The parameters were determined by fitting the data using a robust method of least absolute deviation. The mean absolute deviations for the data are 0.17058377, 0.12586868, and 0.12136768 for J, H, and K_s, respectively. For the magnitudes, $\alpha_1 = 0.00875822$, -0.513155, and -0.0183752, and $\beta_1 = 4.56781$, 4.36025, and 5.11305 for J, H, and K_s, respectively. For the colors, $\alpha_2 = 1.01900$ and 0.969230 and $\beta_2 = -0.238368$ and

0.755103 for $J - H$ and $H - K_s$, respectively. The coefficients β_1 and β_2 include both a zero-point correction and an aperture correction. The derived magnitudes are listed in Table 1. The 10σ limiting magnitudes were approximately 18, 17, and 16 mag for J, H, and K_s, respectively.

3.2. Polarimetry

3.2.1. Linear Polarimetry

Aperture polarimetry of point-like sources in the GGD 27 IRS region was carried out on the combined intensity images for each wave-plate angle at 10 dithered positions per set, instead of using the Stokes Q and U images because the centers of the sources cannot be determined satisfactorily in those images. From the aperture photometry for each wave-plate image, the Stokes parameters for each point-like source were derived as

$$\begin{aligned} Q &= I_0 - I_{45} \\ U &= I_{22.5} - I_{67.5} \end{aligned} \tag{4}$$

where I_a is the intensity with the half-wave plate oriented at a°. The aperture and sky radii were the same as those used in the aperture photometry of the Stokes I images. The degree of polarization P and the polarization position angle θ can be calculated as

$$P_0 = \frac{\sqrt{Q^2 + U^2}}{I} \tag{5}$$

with

$$P_{\mathrm{aperture}} = \sqrt{P_0^2 - \delta P^2} \tag{6}$$

and

$$\theta = \frac{1}{2} \arctan \frac{U}{Q} \tag{7}$$

where δP is the uncertainty in P_0. Since the degree of polarization P is positive, the derived P values tend to be overestimated, especially for sources with a low S/N. Equation (6) was used to correct for this bias (Wardle & Kronberg 1974). To calculate the errors θ_{err} in the polarization position angles, $\theta_{\mathrm{err}} \approx 28\rlap{.}{^\circ}6 \times \delta P/P$ assuming $\delta P \ll P$ was applied (Serkowski 1974, p. 361).

Polarimetry of the extended sources in the GGD 27 IRS region was carried out using the Stokes I, Q, and U images, derived from Equations (1) and (4), as

$$P_{\mathrm{extended}} = \frac{\sqrt{Q^2 + U^2}}{I}. \tag{8}$$

Finally, the degrees of polarization $P_{aperture}$ and $P_{extended}$ and the polarization position angle θ were corrected using the polarization efficiencies and correction angle of SIRPOL, respectively. The polarization efficiencies were 95.5%, 96.3%, and 98.5% in the J, H, and K_s bands, respectively. As described

by Kwon et al. (2010, 2011, 2015), SIRPOL has been routinely used since 2006 and the instrumental polarization is negligible (Kandori et al. 2006; also see Kusune et al. 2015 for updates).

3.2.2. Circular Polarimetry

The Stokes V and I parameters were obtained using

$$V = I_0 - I_{90}$$
$$I = I_0 + I_{90}. \qquad (9)$$
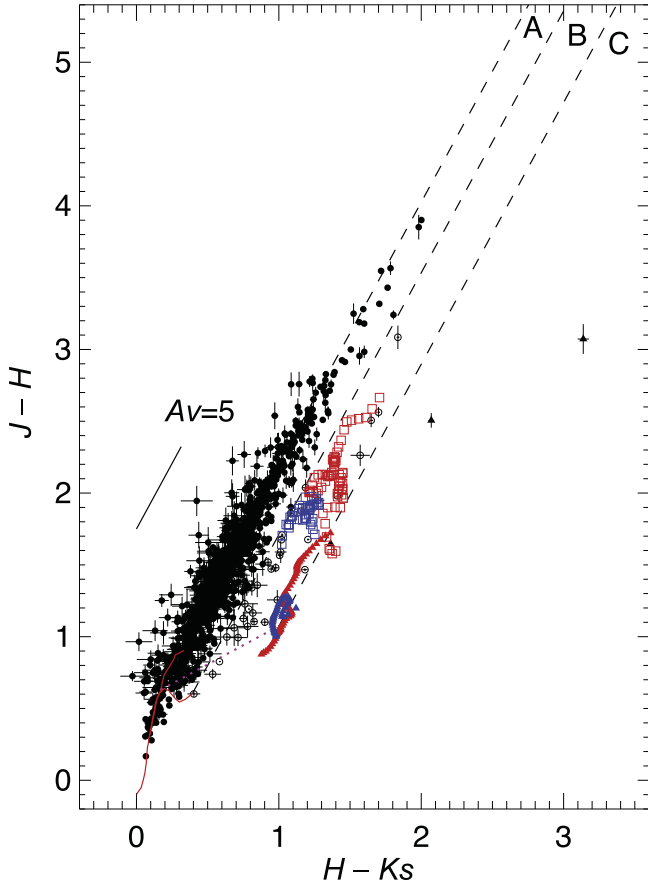
Figure 2. Color–color diagram of point-like sources in the GGD 27 IRS region. Filled circles: group A sources. Open circles: group B sources. Filled triangles: group C sources. Red solid curve: locus of main-sequence and giant stars (Bessell & Brett 1988). Magenta dotted line: locus of classical T Tauri stars (Meyer et al. 1997). Dashed lines: boundaries between domains A, B, and C. Solid line: reddening vector. Red filled triangles: Stokes I magnitude differences to the north of IRS 2. Blue filled triangles: Stokes I magnitude differences to the south of IRS 2. Red boxes: Differences in polarized intensity magnitude to the north of IRS 2. Blue boxes: Differences in polarized intensity magnitude to the south of IRS 2. The colors of GGD 27 IRS are well reproduced by a combination of the colors of a Herbig Ae/Be object with reddening or scattering (Tamura et al. 1997).
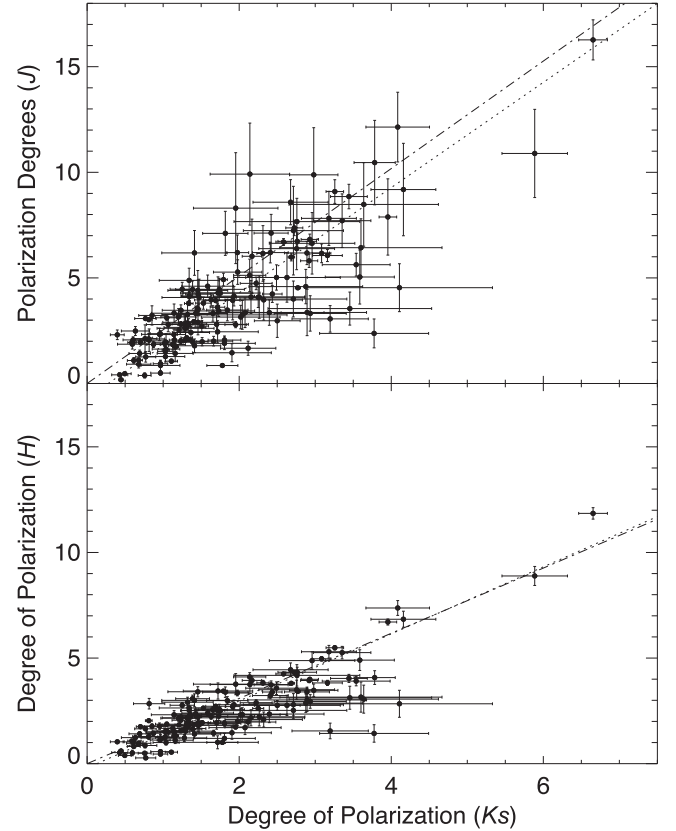

Figure 4. Relationship between degrees of polarization (P_J, P_H, and P_{K_s}) for the 164 sources detected in all three bands. Among the 164 sources, four sources are excluded from the fitting because their errors are larger than the median degree of polarization in one of three bands. A strong correlation between the degrees of polarization is evident. All values are given as percentages (%). Dashed line: general power law $P_\lambda \approx k\lambda^{-1.8}$ for interstellar polarization (Nagata 1990; Martin et al. 1992). Dotted line: linear least-squares approximation.
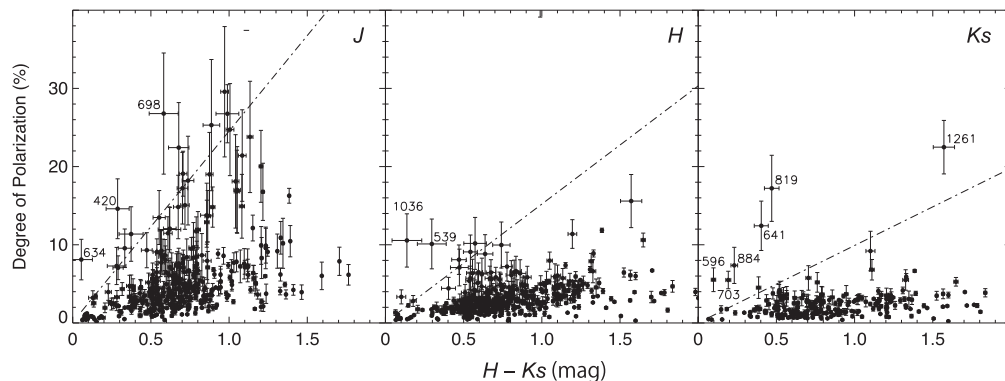

Figure 3. $H - K_s$ color vs. degree of polarization. Several sources with large uncertainties are labeled (see Table 2). Sources 662 and 1261 are located in the GGD 27 IRS nebula, and sources 819 and 641 are located near the nebula. Dotted–dashed lines: empirical upper limits P_{max} (Jones 1989).
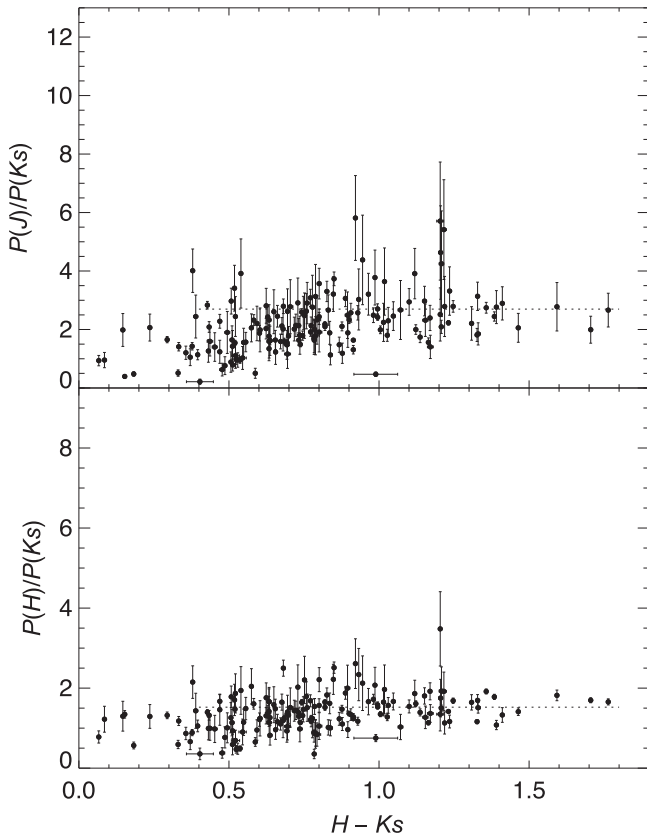
Figure 5. Ratio of J to K_s polarizations (top panel) and of H to K_s polarizations (bottom panel) vs. $H - K_s$ color for 164 sources having $P/\delta P > 3$ in all three bands simultaneously. Dotted lines: weighted averages.
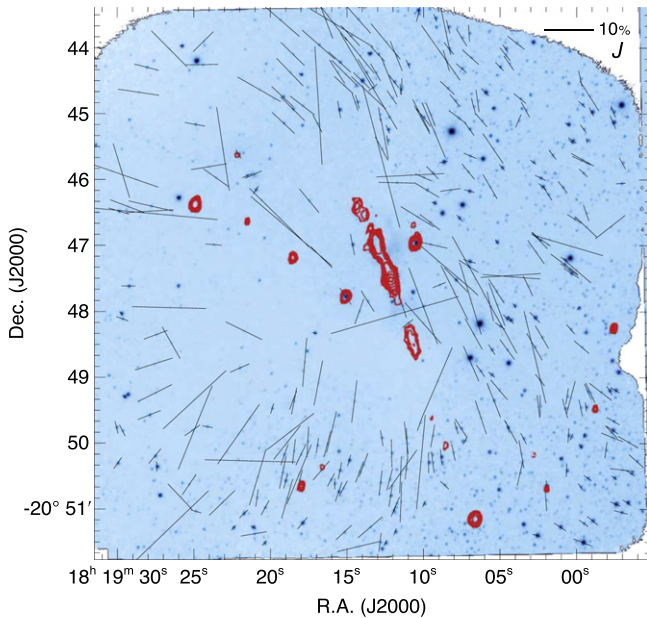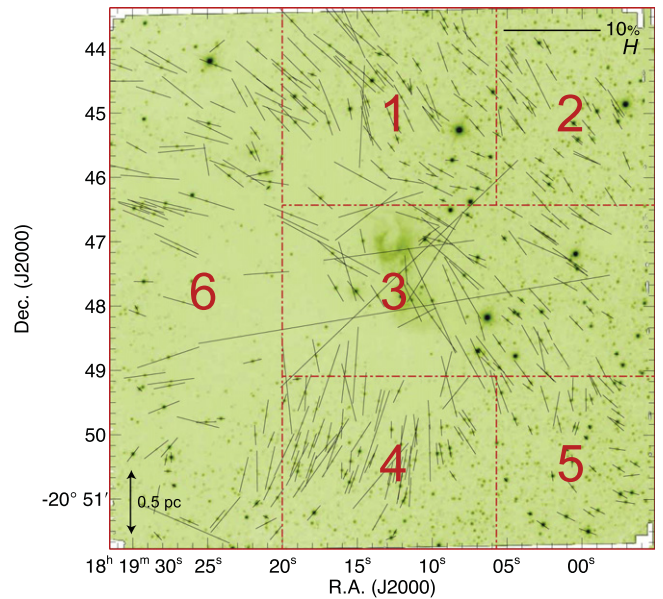

Figure 7. Same as Figure 6 but for the H band. The observed field is divided into six subregions.
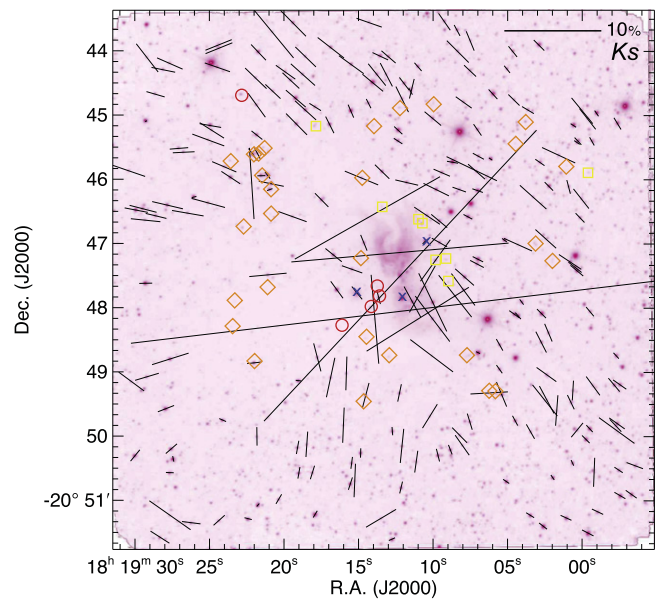

Figure 8. Same as Figure 6 but for the K_s band with protostars (red circles), Class I/II (red triangles), Class II (brown diamonds), and young stellar objects (yellow squares) according to Qiu et al. (2008).

The degree of circular polarization was then calculated as

$$P_{\text{circular}} = V/I \qquad (10)$$

and it was corrected using the polarization efficiencies of SIRPOL, and the standard deviations of 3×3 pixel distributions of P_{circular} are used to determine the error of circular polarization.

4. RESULTS AND DISCUSSION

4.1. Magnetic Field Structure in the GGD 27 IRS Region

One of the problems related to stellar formation concerns the competition between magnetic and turbulent forces (Mac Low
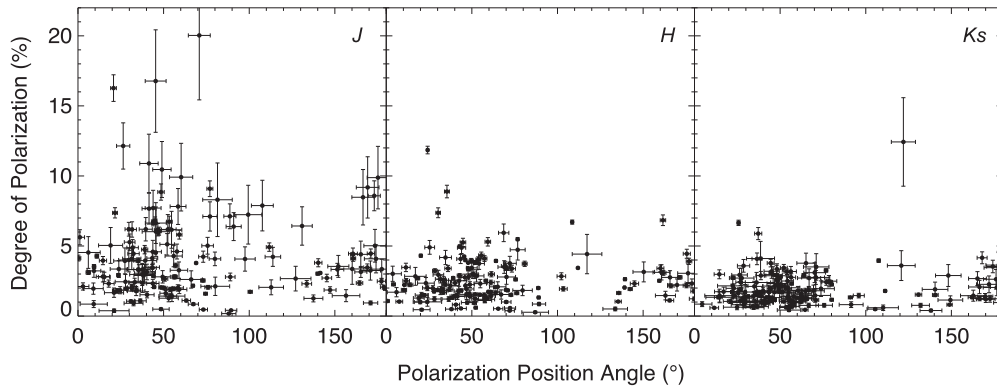

Figure 6. Stokes I image of the J band with polarization vectors for point-like sources having $P/\delta P > 3$. The length of the vectors is proportional to the degree of polarization. Shown in the upper right corner is a 10% vector to set the scale. There are bad pixel clusters around the upper left and upper right corners and in the middle of the right boundary. A composite VLA 6 cm map of the HH 80–81 system by Martí et al. (1993) is superimposed.

Figure 9. Relationship between the position angle and the degree of polarization for 164 sources having $P/\delta P > 3$ detected in all three bands simultaneously. The polarization degree in the data ranges from 0% to 22%.
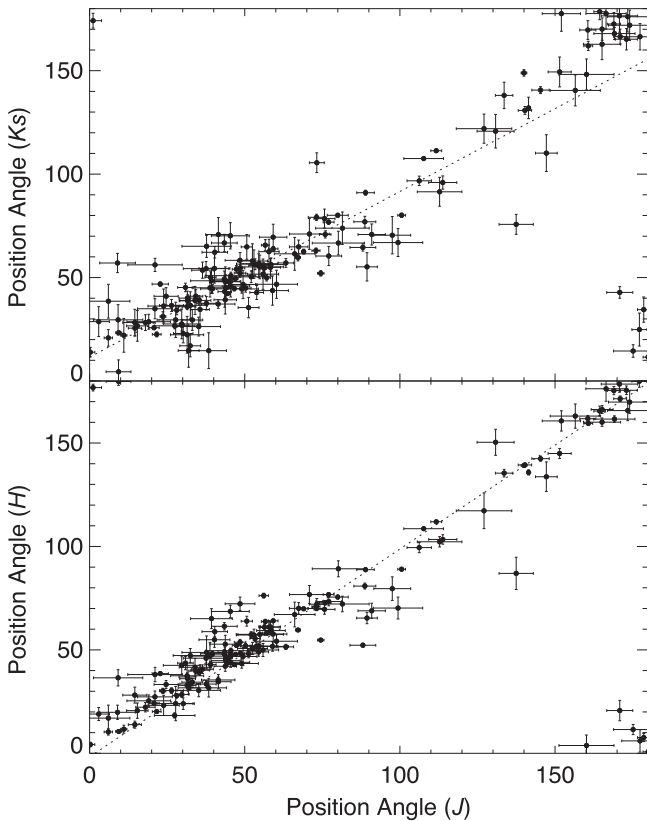

Figure 10. Relationship between polarization position angles (θ_J, θ_H, and θ_{K_s}) for 164 sources having $P/\delta P > 3$ detected in all three bands simultaneously. The position angles are consistent with each other in most cases. Dotted line: $\theta_J = \theta_{K_s}$ on the top panel, $\theta_J = \theta_H$ on the bottom panel.

& Klessen 2004). Therefore it is important to collect magnetic field information in star-forming regions. One method of tracing magnetic fields in dense cloud core regions is near-infrared polarimetry. Previous observational and theoretical studies have shown that near-infrared polarimetry is useful for measuring the dichroic polarization of background stars and embedded sources seen through dense clouds due to the lower extinction at these wavelengths (Davis & Greenstein 1951; Vrba et al. 1976; Wilking et al. 1979; Tamura et al. 1987; Ward-Thompson et al. 2000; Cho & Lazarian 2005; Andersson & Potter 2007, 2010; Kandori et al. 2007; Lazarian 2007; Hough et al. 2008; Kusakabe et al. 2008; Kwon et al. 2010,

2011, 2015; Andersson et al. 2011, 2013; Hoang & Lazarian 2014; Hoang et al. 2015).

In spite of the existence of a prototypical outflow and jet, no observations have previously been made of the magnetic field structures in this region. Both dichroic extinction and scattering processes contribute to the polarization of embedded sources in the GGD 27 IRS region. It is shown here how multiwavelength photometry can discriminate between the two mechanisms and how multiwavelength polarimetry can diagnose dust properties by showing the relationship between the polarization, extinction, and color.

4.1.1. Source Classification and Identification

The magnetic field structure of molecular clouds can be inferred from the near-infrared polarization produced by the dichroic extinction of background stars and embedded YSOs. However, some young objects in clouds also exhibit a substantial degree of intrinsic polarization produced by circumstellar material. A random selection of stars in the direction of a star-forming dense cloud at a distance of approximately 1.7 kpc is likely to produce heavily reddened background stars, a mixture of lightly reddened foreground stars, and YSOs within the cloud showing a large infrared excess. They can be distinguished using multiwavelength photometry as follows.

Figure 2 is a color–color diagram for 1263 sources simultaneously detected in all three bands of Stokes I. The diagram is divided into three domains, allowing sources to be classified into a few groups (Lada & Adams 1992). Sources in domain A are either field stars or YSOs with little infrared excess and substantial reddening. Domain B is adjacent to domain A in the direction of higher $H - K_s$ (to the right) and above the locus of classical T Tauri stars. Sources in domain B are pre-main-sequence stars with infrared excess emission from circumstellar material. Domain C, adjacent to and to the right of domain B, contains infrared protostars and Class I sources. Based on JHK_s photometry, 1226 of the sources are in domain A, 34 in domain B, and three in domain C. Therefore, the majority of our sources are background stars and large intrinsic polarizations are unlikely for these.

4.1.2. Polarization Efficiencies and Near-infrared Dichroic Polarimetry

This section discusses the relationship between near-infrared color and degree of polarization. Jones (1989) has suggested the following empirical relation for the upper limit of the
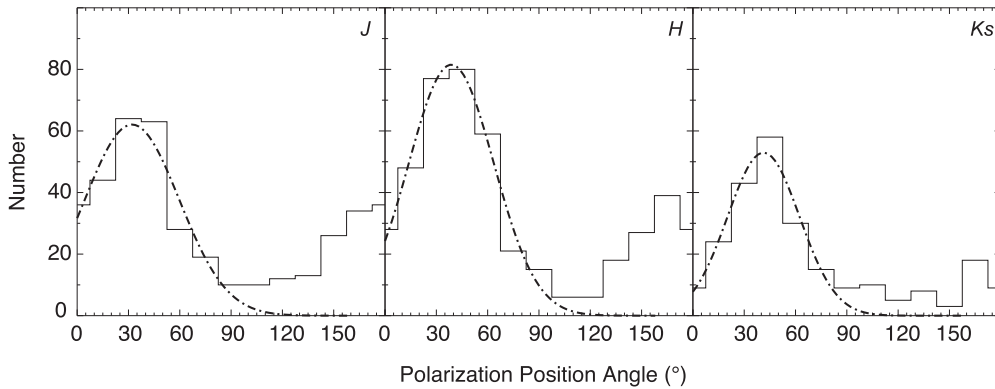
Figure 11. Histograms of the polarization position angles for the J, H, and K_s bands. All of the sources in Table 2 having detectable polarization are included. Dotted–dashed curves: Gaussian fits. The peak angle and dispersion are $32°1$ and $27°7$ for J, $38°7$ and $24°9$ for H, and $41°3$ and $21°1$ for K_s.

interstellar polarization:

$$P_{K,\mathrm{max}} = \tanh\left\{1.5 E(H-K)\frac{1-\eta}{1+\eta}\right\} \qquad (11)$$

where $\eta = 0.875$ and $E(H-K)$ is the reddening arising from extinction. Figure 3 shows the relationship between the $H - K_s$ color and the degree of polarization for the 359, 424, and 232 sources having $P/\delta P > 3$ in the J, H, and K_s bands, respectively. As shown in the figure, most of the sources are within this limit; the few sources above the P_{max} limit have large uncertainties or they are located in the reflection nebula. The value of the slope $P_H/(H-K_s) \approx 4.6$ is comparable to that tracing the magnetic fields in other star-forming regions (Kusakabe et al. 2008; Kwon et al. 2015). The slopes of $P_J/(H-Ks)$ and $P_{K_s}/(H-Ks)$ are approximately 7.0 and 3.9, respectively. The similar slopes suggest that near-infrared polarimetry is a good tracer of magnetic field structures in the GGD 27 IRS region. The near-infrared polarization-to-extinction efficiency of the point-like sources in the GGD 27 IRS region is consistent with that caused by aligned dust grains in the dense interstellar medium. Therefore, the near-infrared polarizations of these sources are probably dominated by dichroic extinction from dust grains aligned with the magnetic field, and the intrinsic polarization, if any, does not significantly affect the observed degree of polarization. However, this result does not completely exclude the possibility that some of the sources have intrinsic polarization because depolarization is also possible.

In addition to the relationship between the near-infrared color and the degree of polarization, there is a relationship between the degrees of polarization (P_J, P_H, and P_{K_s}) for sources having $P/\delta P > 3$ in all three bands. Figure 4 shows a strong correlation between these degrees of polarization, which again supports the dichroic origin of the near-infrared polarization.

4.1.3. Wavelength Dependence of Interstellar Polarization

The wavelength dependence of the polarization can be used to separate the contribution of dichroic extinction from that of any scattering from circumstellar material. In the near-infrared, the polarization due to extinction decreases with wavelength, whereas the polarization due to scattering is not a strong function of wavelength (e.g., Whittet et al. 1992; Casali 1995). Figure 4 shows that there is a correlation between the degrees of polarization P_J, P_H, and P_{K_s} consistent with the general power law $P_\lambda \approx k\lambda^{-1.8}$ for interstellar polarization (Nagata 1990;

Martin et al. 1992). Figure 5 plots the ratio of J to K_s polarizations and the ratio of H to K_s polarizations for sources in the GGD 27 IRS region. There are two groups that exhibit slightly different behavior. One group has $H - K_s < 0.4$, and most of the sources showing small differences at different wavelengths are located in the optically thin southeast. The second group exhibits values in the range of 0.4–1.9 with a fairly constant ratio. The weighted average values are $P_J/P_{K_s} \approx 2.7$ and $P_H/P_{K_s} \approx 1.5$ with standard deviations of 1.0 and 0.5, respectively. These values are consistent with the empirical relation $P \propto \lambda^{-\beta}$, where $\lambda = 1.6$–2.0, and show flattening toward longer wavelengths (Nagata 1990; Martin et al. 1992). Therefore, the polarization of sources having $P/\delta P > 3$ in all three bands can be explained by dichroic extinction. We conclude that most, if not all, of the aperture polarimetry of the point-like sources traces magnetic field structures in GGD 27 up to $A_V \approx 35$ mag based on the color–color diagram.

4.1.4. Magnetic Field Trends

Figures 6–8 are polarization vector maps of point-like sources having $P/\delta P > 3$ superposed on the Stokes I images. Figure 9 plots the relationship between the polarization position angle and the degree of polarization for sources having $P/\delta P > 3$ simultaneously detected in all three bands. For the sources with $P/\delta P > 3$, the position angles (θ_J, θ_H, θ_{K_s}) are consistent with each other in almost all cases (Figure 10). This supports the use of near-infrared polarizations to trace the magnetic field structures in the GGD 27 IRS region. Therefore, the following discussion of magnetic field structures will be principally limited to the H-band data of Figure 7 because these data have the largest number of samples useful for tracing the magnetic fields in the GGD 27 IRS region.

Figure 11 shows histograms and Gaussian fits for the JHK_s polarization position angles of sources having $P/\delta P > 3$. Particular magnetic field directions can be identified from the distribution of position angles. Each of the three histograms has two peaks, with the most notable peak at $30°$–$40°$. To test for a systematic gradient in the magnetic field orientation, the GGD 27 IRS region is divided into six subregions in Figure 7, and Figure 12 presents histograms of the polarization position angles in each of these. The histograms in Regions 1–3 show a peak at $30°$–$40°$, consistent with the peak in the full imaged field, whereas the histograms in Regions 4–6 exhibit other trends. In preparing these histograms, sources having polarizations larger
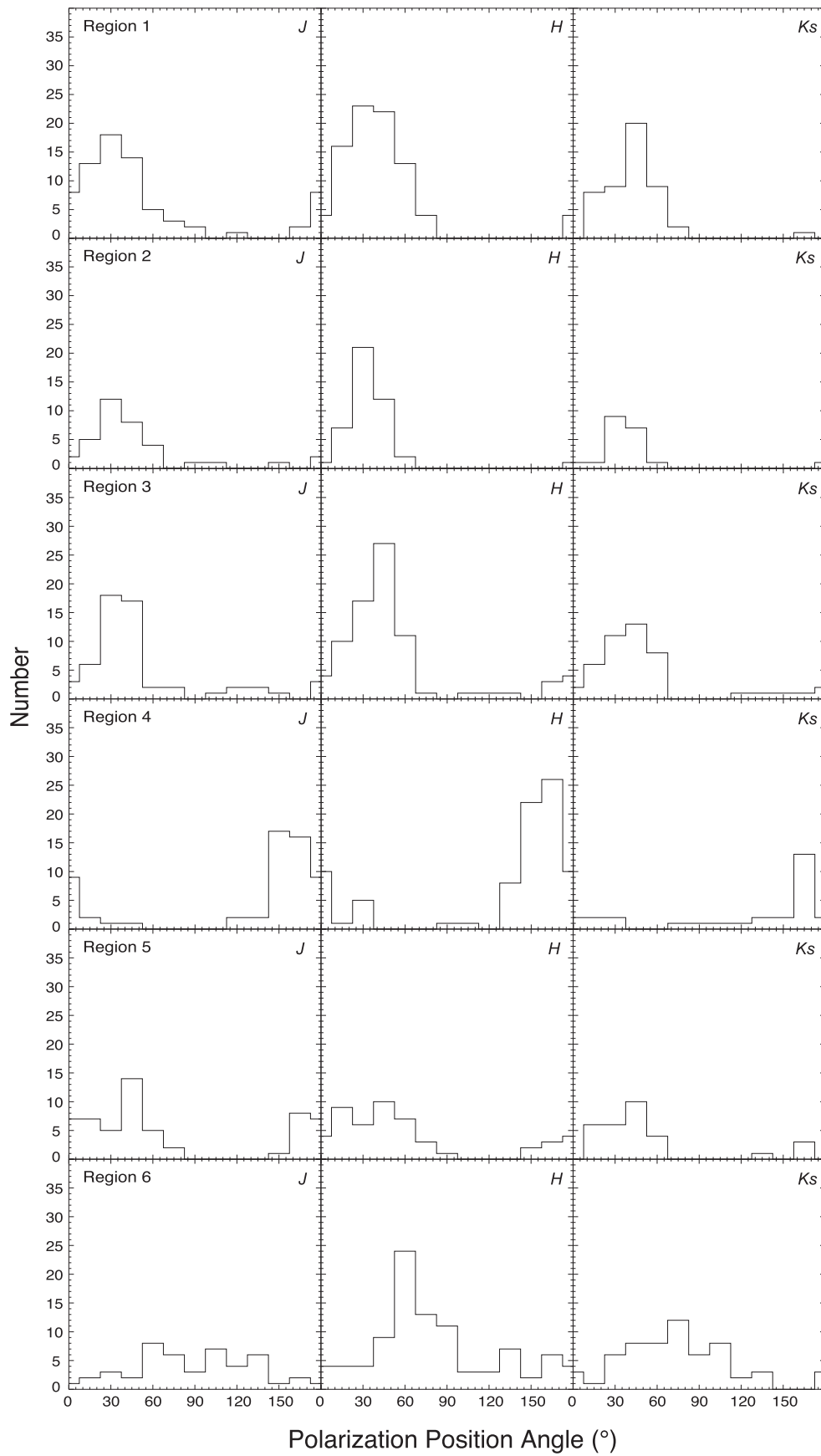
Figure 12. Histograms of polarization position angles for the *J*, *H*, and *K*$_s$ bands. All of the sources in the subregions in Figure 7 have been included.

8

<div align="center">

Table 3
Subregion Information in the GGD 27 IRS Region
</div>

Name	θ_J (deg)	θ_H (deg)	θ_{K_s} (deg)	M. F. Strength[a] at H (μG)	Note
Region 1	45.6 ± 32.9	43.6 ± 18.2	51.1 ± 22.2	~ 90	northern part of the core
Region 2	47.5 ± 28.3	39.7 ± 11.8	43.3 ± 12.0	...	off-core region
Region 3	53.0 ± 33.5	52.8 ± 33.2	54.7 ± 34.4	...	central part of the core
Region 4	122.1 ± 66.9	129.1 ± 61.1	126.1 ± 61.9	...	southern part of the core
Region 5	65.9 ± 54.5	58.9 ± 45.5	62.4 ± 44.4	...	off-core region
Region 6	95.4 ± 40.9	83.9 ± 41.0	76.2 ± 33.1	...	east part of the core

Notes. θ is an average value of polarization position angles for sources having $P/\delta P > 3$ in each band.
[a] M. F. is used as an abbreviation for a magnetic field. Since the Chandrasekhar–Fermi formula, modified by a factor of 0.5, provides accurate estimates of the plane-of-sky field strength for strong fields (when $\delta\theta < 25°$), the magnetic field strength is estimated using the standard deviation of the angle dispersion $\delta\theta$ in the H band when the angle dispersion is small.
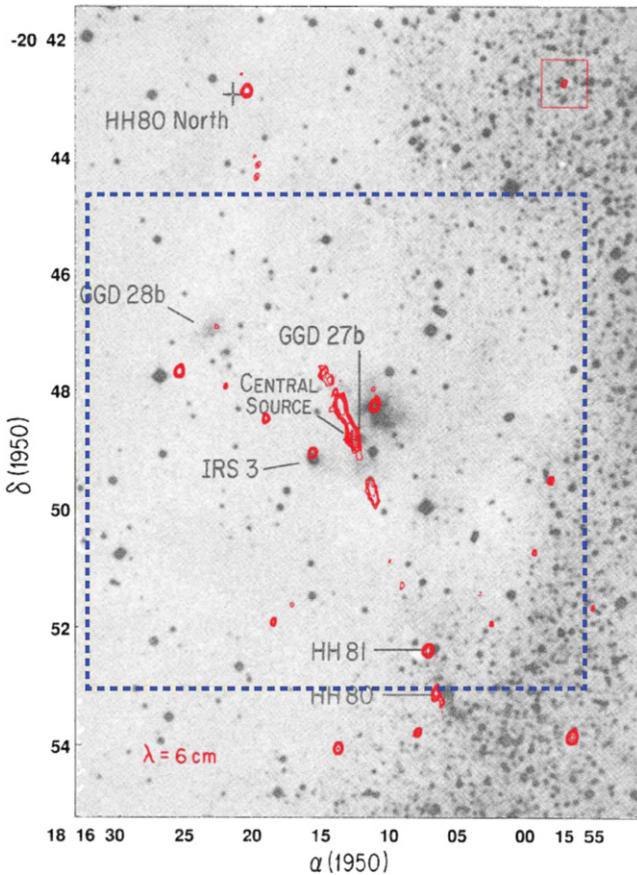

Figure 13. Optical image of HH 80–81 and GGD 27–28 by Martí et al. (1993). A composite VLA 6 cm map of the HH 80–81 system is superimposed on the image. Our near-infrared field of view is indicated by the blue dotted box.

Figure 14. J-band polarization vector map around IRS 2 superimposed on a Stokes I image. The vectors result from 3×3 pixel smoothing and are plotted every nine pixels with intensities greater than 3σ in the J band.

than 8% were excluded, because they are affected by the nebulosities of GGD 27 IRS.

The mean angles in each subregion are summarized in Table 3. Region 1 is the northern part of the core, which presumably traces the magnetic field in the northern part of the outflow. It has well aligned vectors for the magnetic field direction in the northern part of the GGD 27 IRS region. The mean angle is $\sim 44°$ with a standard deviation of $18°$. Region 2 is off-core but the vectors in that region remain well aligned. Its mean angle of $\sim 53°$ with a standard deviation of $12°$ is a bit smaller than that of Region 1. Regions 3–6 show larger angle
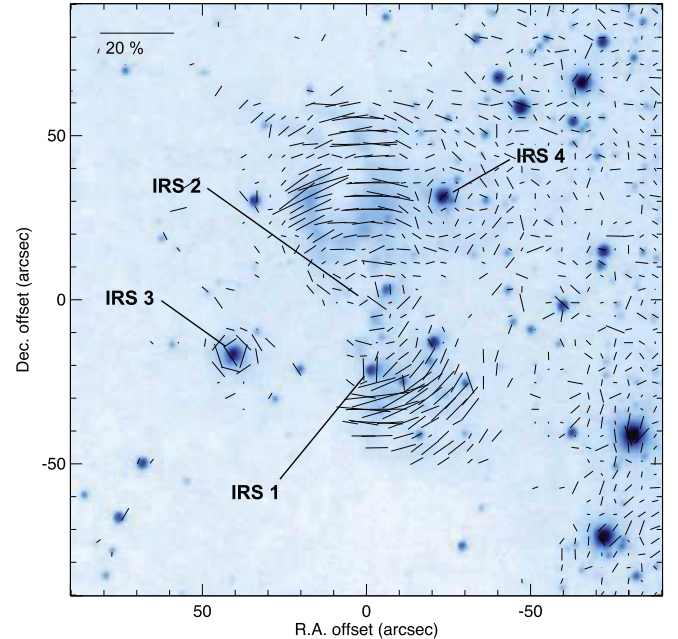
dispersions than those of Regions 1 and 2. Region 3 is the central part of the core including GGD 27 IRS. The vectors in Regions 4–6 appear to be affected by other clouds; the mean angles are approximately $129°$, $59°$, and $84°$, respectively. Region 4 is the southern part of the core, which presumably traces the magnetic field in the southern part of the outflow. Region 5 is another off-core portion, and Region 6 is the eastern part of the core. The existence of other clouds is evident in Figure 13. In the optical image, the blue dotted box indicates the field of observation. Within that field, the west side of GGD 27 IRS is crowded, whereas the east side is obscured by a dark cloud.

There are many protostars, Class I/II, Class II, and YSOs in the observed field. However, their polarizations are mostly undetected (see Figure 8).

4.1.5. Magnetic Field Strength

The method of Chandrasekhar and Fermi can be used to estimate the magnetic field strength by statistically comparing the dispersion in the polarization orientation, although the
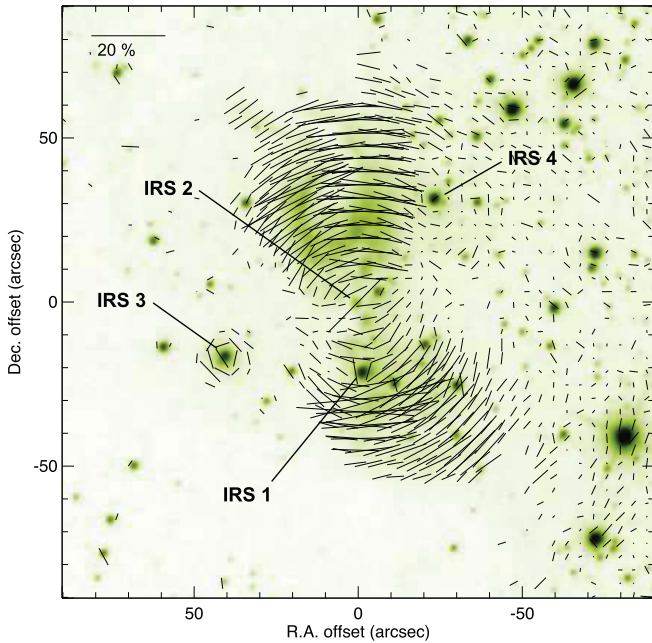
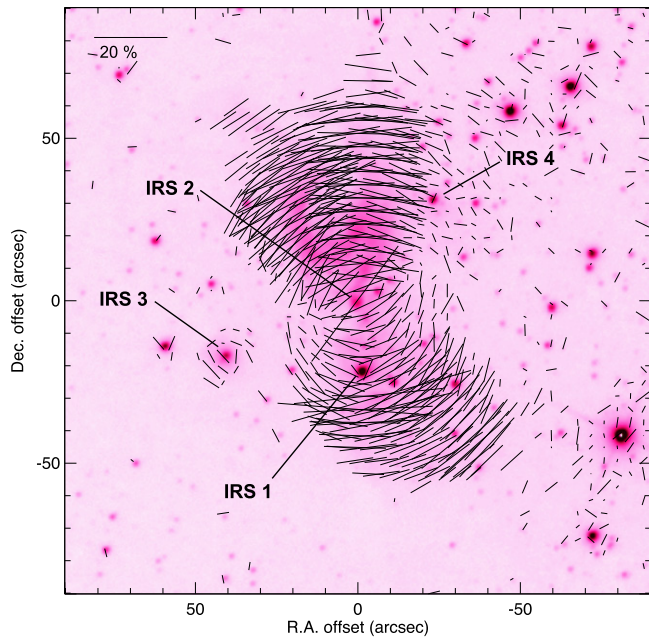**Figure 15.** Same as Figure 14 but for the *H* band.

Figure 16. Same as Figure 14 but for the K_s band.

polarization measurements do not provide a direct estimate of the magnetic field strength at each data point in an image (Chandrasekhar & Fermi 1953). Ostriker et al. (2001) has suggested that $\mathcal{Q} \approx 0.5$ is a good approximation when the angle dispersion is small (say $\delta\theta \lesssim 25°$), based on numerical simulations. Houde (2004) has proposed that a correction factor of ~0.5 is appropriate when the magnetic field is not too weak. Assuming that the velocity perturbations are isotropic, the magnetic field strength projected on the plane of the sky can be expressed as

$$B_p = \mathcal{Q}\sqrt{4\pi\rho}\,\frac{\delta v_{\text{los}}}{\delta\theta} \qquad (12)$$

where $\mathcal{Q}$ is a factor accounting for averaging effects, ρ is the mean density of the cloud, δv_{los} is the rms line-of-sight velocity, and $\delta\theta$ is the dispersion in the polarization angle. To estimate a magnetic field strength in the GGD 27 IRS region, a correction factor of 0.5 is adopted here because the magnetic field appears to be ordered. Then Equation (12) can be rewritten as

$$B_p = 8.5\,\frac{\sqrt{n_{H2}/(10^6\ \text{cm}^{-3})}\ \Delta v\ /(\text{km s}^{-1})^{-1}}{\delta\theta}\ \text{mG} \qquad (13)$$

where n_{H_2} is the number density of hydrogen molecules and Δv is the linewidth. Based on observations of dense $C^{18}O$ (with $J = 1 - 0$), Saito et al. (1999) estimated a local H_2 density of $n_{H_2} = 1.1 \times 10^4\ \text{cm}^{-3}$. They also estimated a linewidth of $\Delta v = 1.8\ \text{km s}^{-1}$ in the GGD 27 IRS region. Using these values with the standard deviation of 18° found in Region 1, the magnetic field strength projected on the plane of the sky is calculated as $B_p \approx 90\ \mu\text{G}$ (see Table 3). Other regions in the core have larger dispersions in the polarization direction, and so their field is less by a factor of 2–3. The estimated magnetic field strength in the GGD 27 IRS region is similar to that in other molecular clouds (namely 20–200 μG) derived using the Chandrasekhar–Fermi method (Andersson & Potter 2005; Poidevin & Bastien 2006; Alves et al. 2008; Kwon et al. 2010, 2011; Sugitani et al. 2011; Kusune et al. 2015).

4.2. Scattered Radiation Field of GGD 27 IRS

Infrared sources in star-forming regions are usually associated with diffuse near-infrared emission, with the diffuse emission generally attributed to scattering of light from a central illuminating source. Such nebulosities, which show centrosymmetric patterns and large degrees of polarization, are called infrared reflection nebulae. Linear polarimetry can reveal infrared reflection nebulae associated with YSOs in star-forming regions, as well as magnetic fields in dark clouds (Whittet et al. 1992; Kwon et al. 2010, 2011, 2015). It has been suggested that there is a strong relationship between the presence of an infrared reflection nebula and CO bipolar outflow, and linear polarimetry of an illuminating source of CO bipolar outflows shows a polarization direction that is perpendicular to the outflow (Hodapp 1984; Sato et al. 1985; Tamura & Sato 1989).

There is a notable infrared reflection nebula around GGD 27 IRS, characterized by both a high degree of polarization and a centrosymmetric pattern of polarization (see Figures 14–16). The fact that significant centrosymmetric patterns are observed around GGD 27 IRS implies that the amount of foreground dichroic extinction is small or patchy. Compared to previous studies, the deeper and wider near-infrared linear polarimetry presented here reveals the detailed morphology of GGD 27 IRS. The present polarization vector map exhibits a centrosymmetric pattern, indicating circumstellar matter such as envelopes or disks. The nebulosity is probably associated with the central source IRS 2 (see Figure 1), which shows highly polarized light at long wavelengths. Interestingly, there are three nebulosity tails to the north of IRS 2, which are bent (see Figure 1). They may be associated with twisted local magnetic fields. In addition to the dominant illuminating source IRS 2, there are other centrosymmetric patterns around IRS 3 and IRS 4. The nebulosity around IRS 4 is particularly notable in the *J* band, which coincides with the optical nebulosity GGD 27.
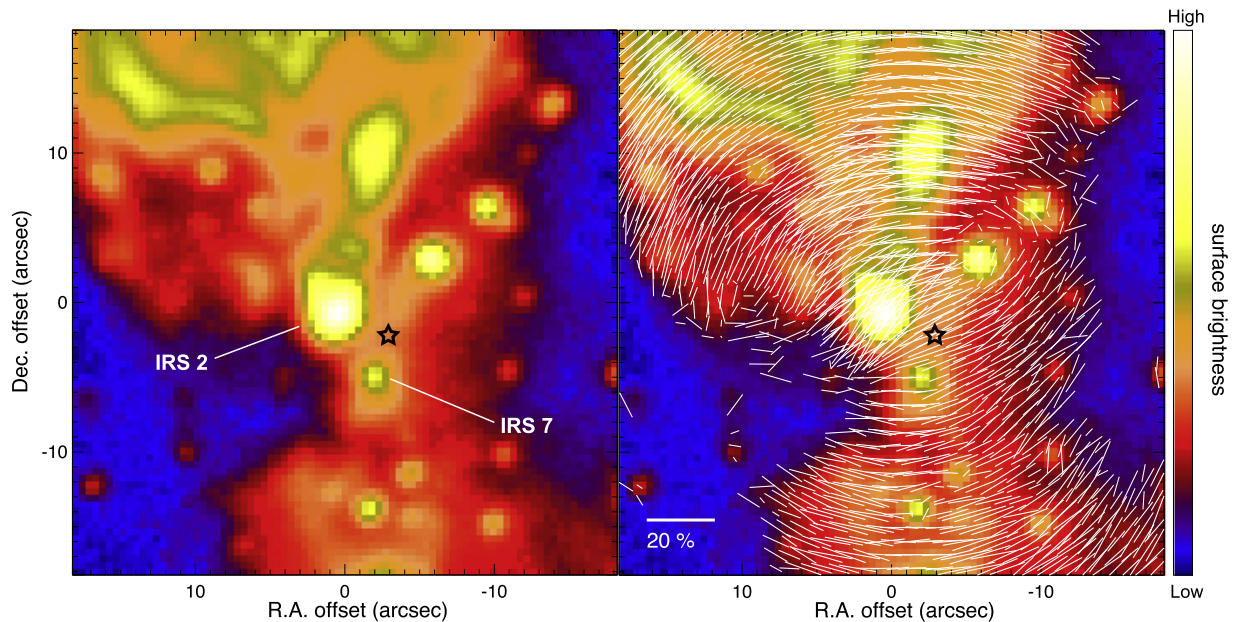
Figure 17. Left panel: Stokes I image of IRS 2 in the K_s band. IRS 2 and IRS 7 are labeled. The location of the 5 GHz radio continuum source of Rodriguez et al. (1980) is marked by a small black star. Right panel: K_s polarization vector map of IRS 2. Shown in the bottom left corner is a 20% vector. The vectors were made by non-smoothing.

The aperture polarimetry of IRS 2 shows high degrees of polarization at JHK_s. These likely originate from a compact circumstellar disk around this massive YSO. In fact this direction of the disk major axis, which shows elongation in the east–west direction (Yamashita et al. 1989), is perpendicular to the radio jet. The direction of aperture polarimetry of IRS 2 is nearly parallel to the elongation of the dense molecular disk delineated by the circumstellar molecular emission (Yamashita et al. 1989).

A color–color diagram for each pixel of the infrared nebulosity is presented in Figure 2. In order to reject pixels having a low S/N, the nebulosity is only plotted in the regions between 70 pixels in the northern part and 40 pixels in the southern part of IRS 2. The polarized intensity images are from the region of the locus of classical T Tauri stars and Herbig Ae/ Be stars known to contain infrared protostars and Class I sources. The plots using Stokes I images are located in domain B, which is believed to contain pre-main-sequence stars with infrared excess emission due to circumstellar material. Therefore, the polarimetric data presented here are consistent with the hypothesis that the nebula represents scattered light from IRS 2, whose "intrinsic" colors are similar to those of Herbig Ae/Be stars with reddening and/or scattering (Tamura et al. 1997).

As mentioned above, the infrared reflection nebula around GGD 27 IRS shows both a high degree of polarization and a centrosymmetric pattern of polarization. However, the possibility of multiple illuminating sources in the vicinity of IRS 2 cannot be ignored because it is also highly polarized relative to other positions near the center of the pattern. Figure 17 shows an enlargement of IRS 2. Based on our polarization pattern, at least two illuminating sources, IRS 2 and IRS 7, can be suggested as the illuminating sources because polarizations are not always centrosymmetric around IRS 2. Note that IRS 7 is considered as a moderately deep embedded young star (Stecklum et al. 1997).

4.3. Circular Polarization in the GGD 27 IRS Region

Figure 18 presents Stokes V and I images showing a region of circular polarization in each band. Positive or negative patterns of circular polarization are especially evident in the northern part of GGD 27 IRS. The extent of the circular polarization is approximately $120''$ ($\sim$1.0 pc), larger even than the circular polarization region of $\sim$0.65 pc in NGC 6334-V (Kwon et al. 2013). A similar pattern is seen in the K_s and H bands, but it is clearest in the K_s band and it is almost invisible in the J band. The pattern of circular polarization increases in clarity with increasing wavelength.

Figure 19 is a K_s-band circular polarization image. The degree of circular polarization in the GGD 27 IRS region is as large as 7%, which is well fitted for the relationship between luminosities and degrees of circular polarization suggested by Kwon et al. (2014). Figure 20 shows Stokes I contours superimposed on the Stokes V image from Figure 18, with the degree of circular polarization marked at various locations. The circular polarization pattern around GGD 27 IRS is typical of what is expected in a bipolar nebula (Kwon et al. 2014), even though the circular polarization pattern is not simple due to its morphology. There are at least two pairs of positive/negative patterns in GGD 27 IRS. In Figure 21, the geometry of GGD 27 IRS is sketched with an inner bright nebula particularly in the northern part and an outer faint nebula surrounding it. Based on the circular polarization images, two bipolar nebulae are expected in this region. One is a small and compact inner nebula, and the other one is a wider but faint outer nebula. This double-shell structure suggests that an episodic outflow event is associated with IRS 2 whose luminosity is $2 \times 10^4 L_\odot$ (Yamashita et al. 1989). Figure 22 shows that the mean polarization (averaged within one resolution element or larger area) still follows the luminosity–circular polarization relation of Kwon et al. (2014), even though the degree of circular polarization is a little lower than expected by the relationship.
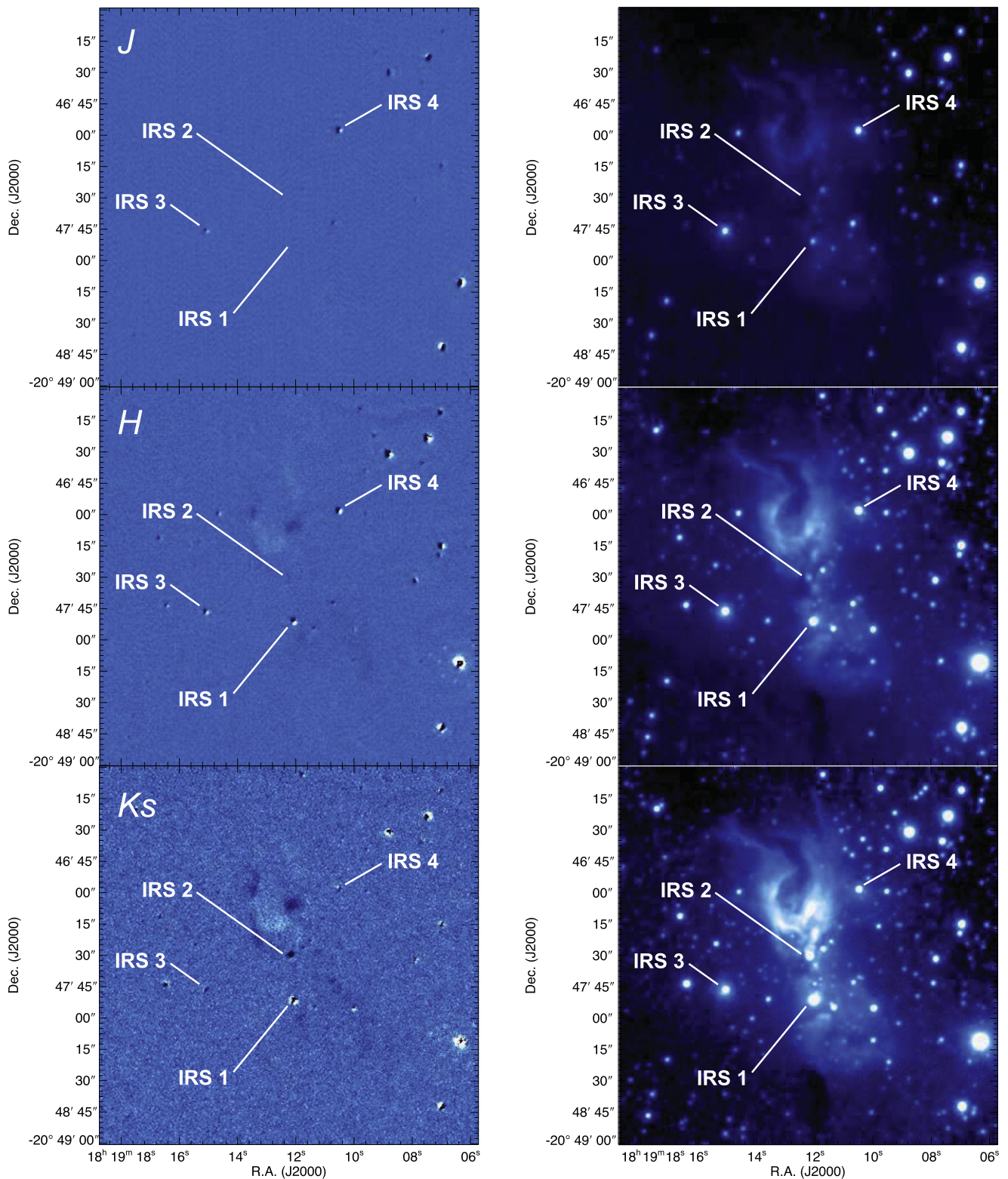
Figure 18. Stokes V and I images in the JHK_s band observed by the IRSF 1.4 m telescope. Left panel: Stokes V images. The white and black colors denote positive and negative values of the Stokes V (in ADU pixel^{-1}), respectively, while the blue background indicates the zero level. Bright point-like sources are not completely canceled in this image. Right panel: Stokes I images at the same scale. Several IRS sources are labeled.

Both the relatively large degrees of polarization and the quadrupole polarization pattern suggest that the origin of the observed circular polarization is likely to be dichoric, which is similar to that in the OMC-1 and NGC 6334-V regions (Fukue et al. 2009; Kwon et al. 2013).

Note that in this paper we suggest that GGD 27 IRS consists of two bipolar nebulae, which could then account for the two-shell structure in circular polarization. Since the structure of an outflow cavity is always complex, high-resolution observations are necessary to confirm this issue.
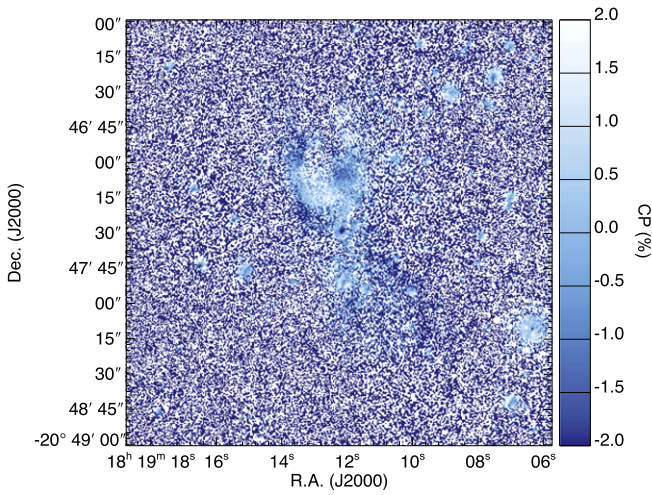
Figure 19. K_s-band circular polarization around GGD 27 IRS. The color code shows the degree of circular polarization as a percentage. The position of IRS 2 is $\alpha = 18^{\rm h}19^{\rm m}11\overset{s}{.}8$, $\delta = -20°47'35''$ [J2000.0].
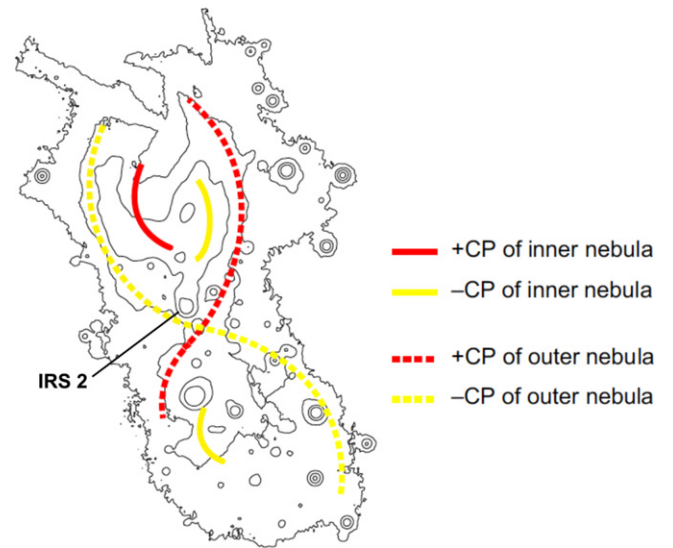

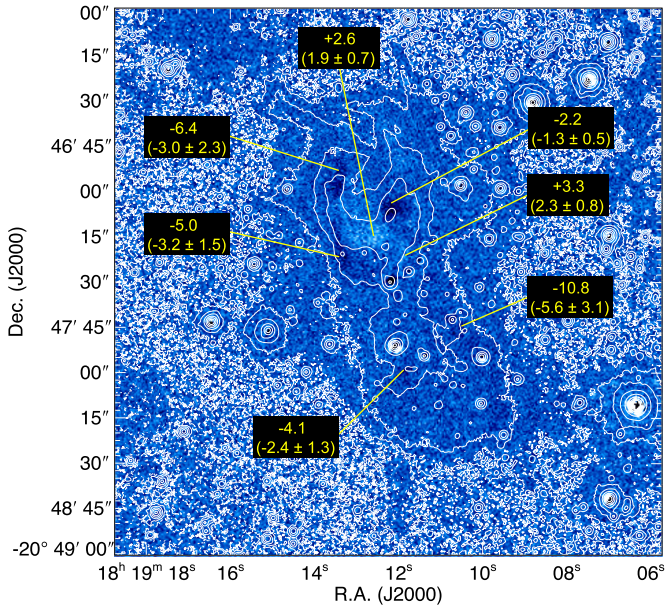**Figure 21.** Hypothesized geometry of GGD 27 IRS for positive (+) and negative (−) circular polarization (CP).

Figure 20. Stokes I contours in the GGD 27 IRS region superimposed on the Stokes V image from Figure 18. The values (on the top in black labels) show the maximum degree of circular polarization at each point, while the values in parentheses (on the bottom in the same label) show the mean degrees of circular polarization (%) with their standard deviation over nine pixels. Since some of regions are very complex, there are gaps between the maximum degree of circular polarization and mean degree of circular polarization in such complex region. The IRS 2 is indicated in Figure 21, with same contours of the central region, i.e., GGD 27 IRS.

5. SUMMARY

Deep and wide-field JHK_s imaging polarimetry has been presented for an $8' \times 8'$ region around GGD 27 IRS in Sagittarius. The main results are as follows.

1. Aperture photometry of 1263 point-like sources detected in all three bands was used to classify them based on a color–color diagram. The polarimetry of the point-like sources enabled the detection of 359, 424, and 232 sources in the J, H, and K_s bands, respectively. Most of
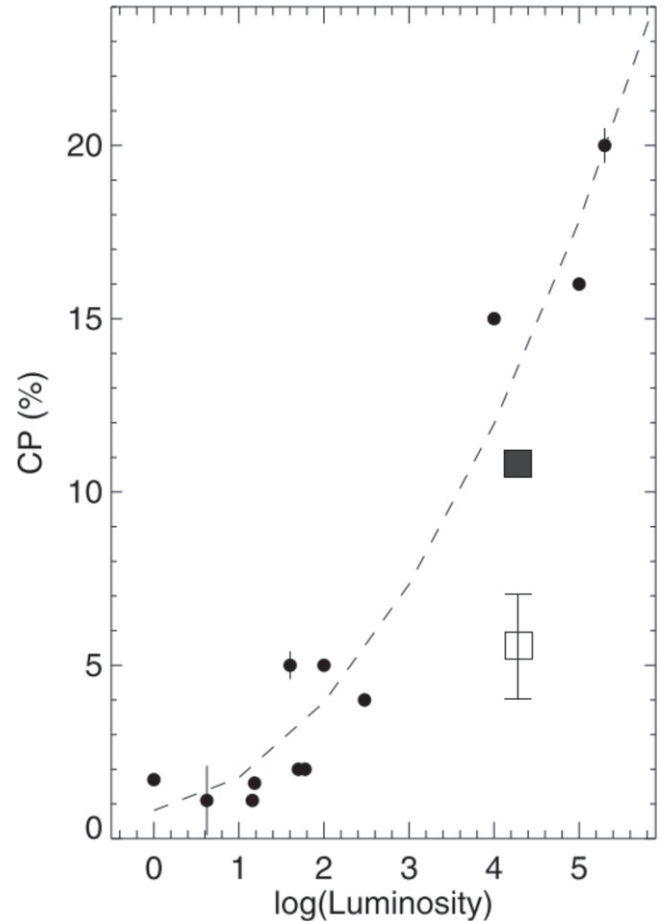

Figure 22. Relationship between the luminosities and circular polarization. The maximum degree of circular polarization (filled square) and mean degree of circular polarization (empty square with an error bar) in the GGD 27 IRS region are overplotted on Figure 3 of Kwon et al. (2014).

the near-infrared polarization of the point-like sources with $P/\delta P > 3$ is dichroic.

2. The sources are primarily expected to be either background stars or pre-main-sequence stars with little

intrinsic polarization. For the 164 sources having $P/\delta P > 3$ in all three bands, the wavelength dependence of the polarization is consistent with dichroic extinction. The local magnetic field in the northern GGD 27 IRS region is centered at approximately $45° \pm 18°$, and the strength of the magnetic field projected on the plane of the sky is estimated to be $\sim 90\,\mu G$ using the Chandrasekhar–Fermi method.

3. The polarization data indicate that an infrared reflection nebula is associated with GGD 27 IRS. That conclusion is consistent with previous studies, but more detailed and extended structures have been found here.

4. The circular polarization, which is as large as 11% in one pixel or $5.6 \pm 3.1\%$ over nine pixels, provides detailed images for this region and shows two overlapping outflows. The maximum extent of the circular polarization around GGD 27 IRS is approximately $120''$ (1.0 pc), which is the largest extent ever observed. Combined with previous circular polarization measurements, the present data suggest the universality of extended (parsec-sized) left- and right-handed circular polarization zones in star-forming regions.

REFERENCES

Alves, F. O., Franco, G. A. P., & Girart, J. M. 2008, A&A, 486, L13
Andersson, B.-G., Piirola, V., De Buizer, J., et al. 2013, ApJ, 775, 84
Andersson, B.-G., Pintado, O., Potter, S. B., Straižys, V., & Charcos-Llorens, M. 2011, A&A, 534, 19
Andersson, B.-G., & Potter, S. B. 2005, MNRAS, 356, 1088
Andersson, B.-G., & Potter, S. B. 2007, ApJ, 665, 369
Andersson, B.-G., & Potter, S. B. 2010, ApJ, 720, 1045
Aspin, C., Casali, M. M., Geballe, T. R., & McCaughrean, M. J. 1991, A&A, 252, 299
Bessell, M. S., & Brett, J. M. 1988, PASP, 100, 1134
Casali, M. M. 1995, MNRAS, 277, 1385
Chandrasekhar, S., & Fermi, E. 1953, ApJ, 118, 113
Cho, J., & Lazarian, A. 2005, ApJ, 631, 361
Chrysostomou, A., Lucas, P. W., & Hough, J. H. 2007, Natur, 450, 71
Davis, L., & Greenstein, J. L. 1951, ApJ, 114, 206
Fukue, T., Tamura, M., Kandori, R., et al. 2009, ApJL, 692, L88
Hoang, T., & Lazarian, A. 2014, MNRAS, 438, 680
Hoang, T., Lazarian, A., & Andersson, B.-G. 2015, MNRAS, 448, 1178
Hodapp, K.-W. 1984, A&A, 141, 255
Houde, M. 2004, ApJL, 616, L111
Hough, J. H., Aitken, D. K., Whittet, D. C. B., Adamson, A. J., & Chrysostomou, A. 2008, MNRAS, 387, 797
Jones, T. J. 1989, ApJ, 346, 728
Kandori, R., Kusakabe, N., Tamura, M., et al. 2006, Proc. SPIE, 6269, 626951
Kandori, R., Tamura, M., Kusakabe, N., et al. 2007, PASJ, 59, 487
Kusakabe, N., Tamura, M., Kandori, R., et al. 2008, AJ, 136, 621
Kusune, T., Sugitani, K., Miao, J., et al. 2015, ApJ, 798, 60
Kwon, J., Choi, M., Pak, S., et al. 2010, ApJ, 708, 758
Kwon, J., Tamura, M., Hough, J. H., et al. 2014, ApJL, 795, L16
Kwon, J., Tamura, M., Hough, J. H., et al. 2015, ApJS, 220, 17
Kwon, J., Tamura, M., Kandori, R., et al. 2011, ApJ, 741, 35
Kwon, J., Tamura, M., Lucas, P. W., et al. 2013, ApJL, 765, L6
Lada, C. J., & Adams, F. C. 1992, ApJ, 393, 178
Lazarian, A. 2007, JQSRT, 106, 225
Lynds, B. T. 1962, ApJS, 7, 1
Mac Low, M.-M., & Klessen, R. S. 2004, RvMP, 76, 125
Martí, J., Rodríguez, L. F., & Reipurth, B. 1993, ApJ, 416, 208
Martin, P. G., Adamson, A. J., Whittet, D. C. B., et al. 1992, ApJ, 392, 691
Masqué, J. M., Girart, J. M., Estalella, R., Rodriguez, L. F., & Beltrán, M. T. 2012, ApJL, 758, L10
Meyer, M. R., Calvet, N., & Hillenbrand, L. A. 1997, AJ, 114, 288
Nagata, T. 1990, ApJL, 348, L13
Nagayama, T., Nagashima, C., Nakajima, Y., et al. 2003, Proc. SPIE, 4841, 459
Ostriker, E. C., Stone, J. M., & Gammie, C. F. 2001, ApJ, 546, 980
Poidevin, F., & Bastien, P. 2006, ApJ, 650, 945
Qiu, K., Zhang, Q., Megeath, S. T., et al. 2008, ApJ, 685, 1005
Reipurth, B., & Graham, J. A. 1988, A&A, 202, 219
Rodríguez, L. F., Moran, J. M., Ho, P. T. P., & Gottlieb, E. W. 1980, ApJ, 235, 845
Saito, H., Tachihara, K., Onishi, T., et al. 1999, PASJ, 51, 819
Sato, S., Nagata, T., Nakajima, T., et al. 1985, ApJ, 291, 708
Serkowski, K. 1974, Astrophysics. Part A: Optical and Infrared, Vol. 12 (Science Direct)
Stecklum, B., Feldt, M., Richichi, A., Calamai, G., & Lagage, P. O. 1997, ApJ, 479, 339
Stetson, P. B. 1987, PASP, 99, 191
Sugitani, K., Nakamura, F., Watanabe, M., et al. 2011, ApJ, 734, 63
Tamura, M., Gatley, I., Joyce, R. R., et al. 1991, ApJ, 378, 611
Tamura, M., Hough, J. H., Chrysostomou, A., et al. 1997, MNRAS, 287, 894
Tamura, M., Nagata, T., Sato, S., & Tanaka, M. 1987, MNRAS, 224, 413
Tamura, M., & Sato, S. 1989, AJ, 98, 1368
Vrba, F. J., Strom, S. E., & Strom, K. M. 1976, AJ, 81, 958
Ward-Thompson, D., Kirk, J. M., Crutcher, R. M., et al. 2000, ApJL, 537, L135
Wardle, J. F. C., & Kronberg, P. P. 1974, ApJ, 194, 249
Whittet, D. C. B., Martin, P. G., Hough, J. H., et al. 1992, ApJ, 386, 562
Wilking, B. A., Lebofsky, M. J., Rieke, G. H., & Kemp, J. C. 1979, AJ, 84, 199
Yamashita, T., Hayashi, S. S., Kaifu, N., et al. 1989, ApJ, 347, 894
Yamashita, T., Sato, S., Nagata, T., et al. 1987, A&A, 177, 258